Soft Matter

Specific Deformation Behavior of Isotactic Polypropylene Films under Multiaxial Stress Field

Journal:	*Soft Matter*
Manuscript ID	SM-ART-01-2022-000147.R1
Article Type:	Paper
Date Submitted by the Author:	01-Apr-2022
Complete List of Authors:	Kojio, Ken; Kyushu University, Fujimoto, Aya; Kyushu University Nagano, Chigusa; Kyushu University Nozaki, Shuhei; Kyushu University Yokomachi, Kazutoshi; Kyushu University Kamitani, Kazutaka; Kyushu University Watanabe, Hirohmi; Kyushu University Takahara, Atsushi; Kyushu University

Submitted to *Soft Matter*

Specific Deformation Behavior of Isotactic Polypropylene Films under Multiaxial Stress Field

Ken Kojio[1,2,3*], Aya Fujimoto[1], Chigusa Nagano[2], Shuhei Nozaki[2],
Kazutoshi Yokomachi[1], Kazutaka Kamitani[1], Hirohmi Watanabe[1], Atsushi Takahara[1,2*]

[1]Institute for Materials Chemistry and Engineering, [2]Graduate School of Engineering,
[3]WPI-I[2]CNER, Kyushu University
744 Motooka, Nishi-ku, Fukuoka, 819-0395, Japan
Phone: +81-92-802-2517, Fax: +81-92-802-2518

*Authors to whom correspondence should be addressed.
kojio@cstf.kyushu-u.ac.jp
takahara.atsushi.150@m.kyushu-u.ac.jp

Abstract

The specific deformation behavior of crystalline polymer films, namely unoriented crystallized isotactic polypropylene (*it* PP) films, was investigated under a multiaxial stress field. Changes in the aggregation structure of the films were investigated during the bulge deformation process using *in situ* small-angle X-ray scattering, wide-angle X-ray diffraction (WAXD) measurements, and polarized high-speed-camera observations. The films had a thickness of approximately 10 μm. The *it* PP films were fixed at the hole of a plate, then bulge deformation was applied using N_2 or He gas pressure, and stress-strain curves were then calculated from the applied pressure and bulge height. Yielding was observed in the stress-strain curves. Below the yield point, *in-situ* WAXD measurements revealed that the crystal lattice expanded isotropically at the center, edge, and bottom of the bulge hole. Above the yield point, a craze started to form slightly near the center, and crazes formed in various directions with a further increase in strain, while the crystal lattice expanded uniaxially along the circumference at the edge and bottom. Crazes oriented in various directions merged and lost birefringence, indicating a change to the isotropic orientation. The different directions of the crazes indicated several directions of stress. In other words, even if multiaxial deformation is applied to a crystalline *it* PP film, the string-shaped crystalline polymer chain structure produces local anisotropic uniaxial stress.

Introduction

Polyolefins have gained significant research interest because of their reasonable price, high processibility, low toxicity, low density, high strength, high waterproofing ability, and high chemical resistance.[1] Increasing the toughness of polyolefins is crucial to expand their applications. For instance, polyolefin separator films, such as polyethylene and polypropylene films, in lithium-ion batteries must be substantially thin and tough to achieve battery weight reduction.[2] Since cavitation can lighten materials and improve impact resistance, investigations of cavitation distributions in porous isotactic polypropylene (*it* PP) films have been performed based on X-ray scattering and diffraction to control the mechanical properties.[3-5]

Uniaxial stretching deformation is one of the most prevalent mechanical deformation methods used to evaluate the mechanical properties of polymers. This is because the measurement can be performed simply, and the instrument is commercially available. There are some reports on the in situ structure analysis of *it* PP during uniaxial deformation to clarify the relationship between the structure and mechanical properties.[6-12] Nozue et al. reported the deformation behavior of *it* PP spherulite films during uniaxial stretching by simultaneous small-angle X-ray scattering (SAXS), wide-angle diffraction (WAXD), and polarized optical microscopy (POM).[11] Notably, they revealed structural information on parent and daughter lamellae in various orientations. Furthermore, using Raman spectroscopy, Kida revealed a change in the molecular aggregation state during uniaxial deformation.[10] However, the uniaxial deformation mode does not accurately simulate practical conditions.

The importance of multiaxial deformation, such as biaxial[13-20], compression[21], bulge[22], lateral indentation [23], and flow[24], in terms of understanding the physical properties of polymers is well known. This is because (1) the polymers have a string-shaped structure, (2) they can become entangled, and (3) the strain density energy function of the materials can be obtained. Among these deformation modes, bulge testing has some unique features: specimens with a small size and low thickness are sufficient, the entire deformation can be monitored during the deformation process, and the reliability of the mechanical data is relatively high. There have been some reports on the investigation of mechanical properties using the bulge testing of polymer films.[25-31] By contrast, we recently developed a bulge tester that can evaluate the molecular aggregation structure of polymer

films during bulge deformation using polarized high-speed camera observations, optical microscopy, synchrotron radiation wide-angle X–ray diffraction (WAXD), and Fourier transform infrared spectroscopic measurements.[32, 33] It was revealed that the crystal lattice of isothermally crystallized and quenched Nylon12 films exhibited elastic and slightly plastic responses under bulge deformation, respectively.[32] In addition, the deformation and rupture mechanisms of poly(methyl methacrylate) and polycarbonate films in the glassy state were investigated using in-situ measurements.[33] Furthermore, it was revealed that the stress field during bulge testing is multiaxial with regard to the center of the bulge chamber hole. Because polymer chains have an anisotropic structure, it is indispensable to evaluate their deformation behavior under multiaxial stresses.

In this study, we chose crystalline *it* PP with a flexible nature and prepared films with no crystal orientation. This is because the orientation change in molecular chains is enhanced during bulge testing. The molecular aggregation state of the *it* PP films was investigated by bulge testing using *in-situ* synchrotron radiation WAXD and SAXS measurements, polarized optical microscopy (POM), and polarized high-speed camera observations. Finally, the difference between bulge and uniaxial deformation was discussed.

Experimental

Film preparation

it PP was purchased from Sigma-Aldrich, and its number-averaged molecular weight and weight-averaged molecular weight were 67,000 and 250,000 g/mol, respectively. *it* PP films were prepared at a pressure of 5 MPa using a hot press. The thickness of all the films was set to ca. 10 μm. The samples were heated to 190 °C, which is above the melting temperature (T_m=165 °C), and then quenched using a metal plate to obtain unoriented crystalline *it* PP films. The glass transition temperature of *it* PP is ca. -10 °C.

Bulge deformation test

Figure S1 shows the setup used for the bulge test of the films. The films were fixed in a hole of a lab-made bulge chamber with a diameter of 2 or 3 mm; subsequently, N_2 or He gas was applied at 25 ºC. The film height was measured by a surface-scanning laser confocal displacement meter (LT-9010M, Keyence, Co.) and direct observation from the lateral direction through a polished

quartz sample holder. The applied gas pressure was adjusted using a digital mass flow meter (F-201CV-100-RAD-11-V, Bronkhorst High), controlled by a digital pressure controller (P-702CV-21KR-RAD-11-V, Bronkhorst High). The maximum pressure was 800 kPa. Then, stress-strain curves were obtained from the relationship between the applied pressure and actual film height (bulge height) using the following equations[22]:

$$\text{Stress: } \sigma = \frac{PR}{2t} = \frac{P(a^2 + h^2)}{4th} \quad (1)$$

$$\text{Strain: } \varepsilon = \frac{s - s_0}{s_0} \quad (2)$$

$$\mathrm{s} = \theta R = \tan^{-1}\left(\frac{h}{a}\right)\frac{2(a^2 + h^2)}{h} \quad (3)$$

where s is the arc length, s_0 is the initial arc length, P is the applied pressure, h is the bulge height, t is the sample thickness, a is the film radius, θ and R are the angle and bulge radius of curvature, respectively. To obtain accurate camera length for WAXD at each position and the accuracy of bulge height, side view observation was carried out. Figure S2 shows the side view images of the *it* PP films at various strains. The film seems to keep an arc shape by the strain of 0.17. Since almost of the strain data shown in this study is in the range from 0 to 0.2, all data are quantitative enough for discussion.

***In situ* molecular aggregation structure analyses**

In situ wide-angle X-ray diffraction (WAXD) and small-angle scattering (SAXS) measurements were carried out at the BL40XU and BL05XU beamlines at SPring-8 to evaluate the aggregation structure of the *it* PP film during bulge deformation. The wavelength and size of the X-ray beam were set to be 0.1 nm and 100 μm x 200 μm, respectively. A CCD (ORCA-Flash4.0, Hamamatsu Photonics), PILATUS 100k (DECTRIS, Ltd.), and PILATUS 1M (DECTRIS, Ltd.) were used as detectors to measure the diffracted/scattered X-rays, with camera lengths of 100 mm and 2 m, respectively. The WAXD and SAXS data were collected with exposure times of 500 or 2000 ms and 500 ms, respectively, every 2 s. Since the pressure rate was ca. 80 kPa min^{-1} and the maximum pressure is ca. 300 kPa, it took ca. 200 s to attain the rupture. Thus, the structure relaxation of the *it* PP film can be ignored. Data processing, such as control of the contrast of 2D-patterns and preparation of 1D-profiles for the obtained 2D-patterns, was performed using the FIT-2D software (Ver. 12.077; Andy Hammersley/ESRF, Grenoble, France).

Ultra-small-angle X-ray scattering (USAXS) was performed to evaluate the structural change

of the *it* PP film at the micrometer scale after bulge deformation. The wavelength and size of the X-rays were set to 0.054 nm and 200 μm x 200 μm, respectively. A PILATUS 100k was used as a detector to measure the scattered X-rays, and the camera length was 160 m.

The orientations of the molecular chains and functional groups in the *it* PP films are closely related to the refractive index. The refractive index and direction of the short axis of the refractive ellipsoid were observed using a polarized high-speed camera (CRYSTA PI-1P, PHOTRON LTD., Japan), and circularly polarized 520 nm light was used. The polarization directions of the four adjacent microtip detectors were 0°, 45°, 90 °, and 135°. The frame rate was 60 and 420,000 fps for the top view and side view, respectively, in this study. The spatial resolution of the 50x objective lens was approximately 1 μm. This observation was made for the *it* PP film during the bulge and uniaxial stretching deformation processes.

Results and discussion

Below yield point

Figure 1 shows the stress-strain curves obtained by bulge testing of the *it* PP films with a thickness of 8 μm. The modulus obtained from the initial slope of the stress-strain curves was 1 GPa.

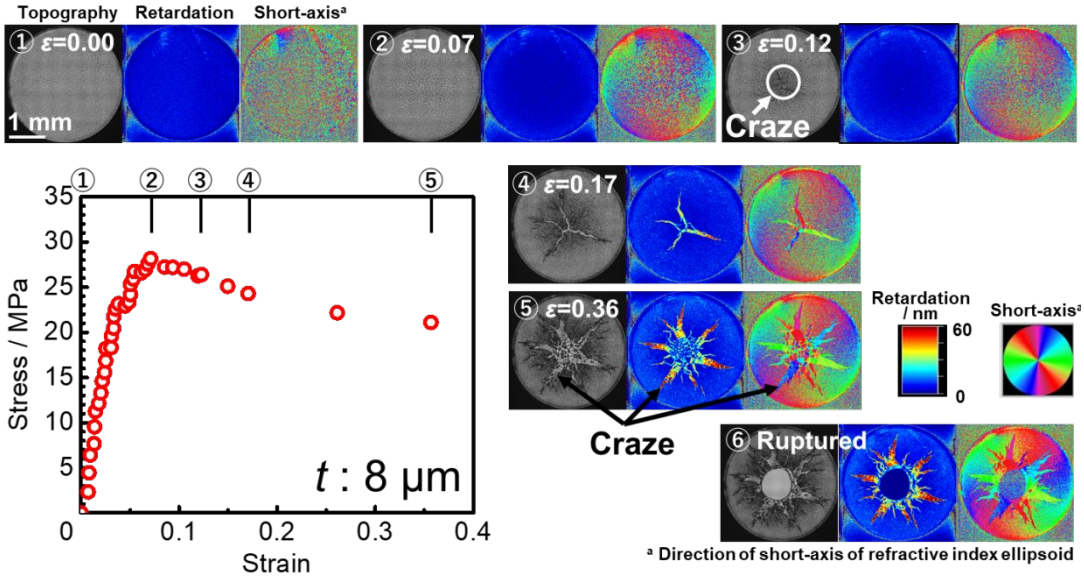

Figure 1. Stress-strain curves of isotactic polypropylene films with a thickness of 8 μm obtained by bulge testing and polarized high-speed camera images at various strains. The three inset images correspond to topography, retardation, and the direction of short-axis of the refractive index ellipsoid from left to right.

This magnitude is comparable to that obtained by uniaxial stretching deformation. Yield behavior was clearly observed at a strain of 0.06 and at a stress of 27 MPa. Such behavior may be related to the formation of an anisotropic craze. A more detailed discussion on the images provided in Figure 1 will be presented in a later section.

Figure 2 shows WAXD profiles of *it* PP films with a thickness of 10 μm obtained in the initial state during bulge testing at the center of the hole. The *it* PP films prepared in this study showed crystalline peaks at scattering vectors (q) of 9.9, 11.9, 13.1, 14.9, and 15.4 nm^{-1} in the initial state. These peaks can be assigned to the (110), (040), (130), (111), (131), and (041) planes of the α phase of the *it* PP films. With an increase in strain, all crystalline peaks shifted to a lower q. This indicates that the crystalline lattice in the *it* PP films isotropically expanded by bulge deformation at the center of the bulge hole. A similar trend was observed even for the edge and bottom of the hole. To investigate the anisotropy of deformation of the crystal lattice depending on the position within the bulge hole, WAXD profiles along the transverse and longitudinal directions at three positions—the center, bottom, and right—were compared. Figure 3 shows the relationship between film strain and

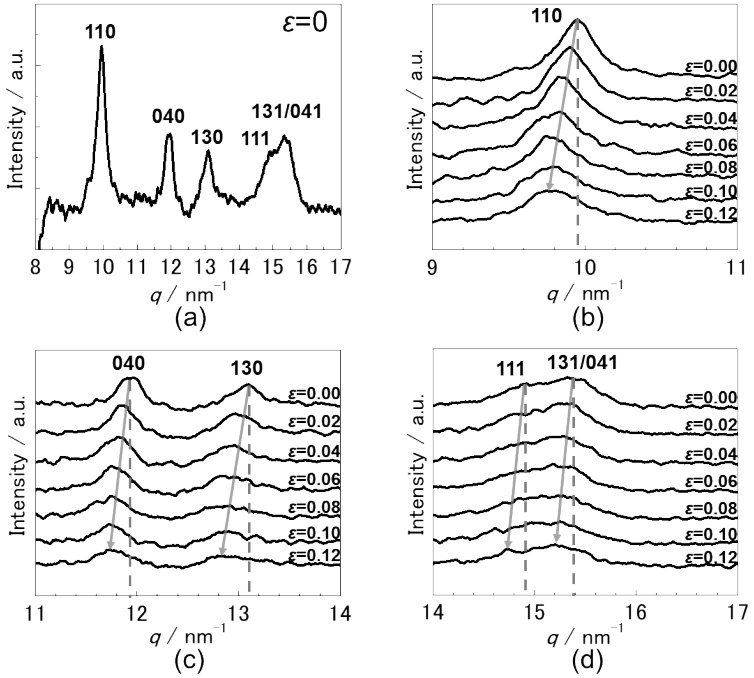

Figure 2. WAXD profiles of *it* PP films with a thickness of 10 μm obtained during bulge testing at the center of the film. (a) $8 < q < 17$ nm^{-1} at the initial state. (b) $9 < q < 11$ nm^{-1} , (c) $11 < q < 14$ nm^{-1} , (d) $14 < q < 17$ nm^{-1} with an increase in strain from 0 to 0.12.

strain obtained by WAXD profiles ($\varepsilon_{(hkl)}$) along the transverse and longitudinal directions at three positions in the bulge hole. For the center position (A), the strain obtained from the (110) and (131)/(041) planes in the WAXD profiles ($\varepsilon_{(110)}$ and $\varepsilon_{(131)/(041)}$) increases with an increase in film strain for both the transverse and longitudinal directions. At around the yield point, $\varepsilon_{(110)}$ and $\varepsilon_{(131)/(041)}$ showed constant values. On the contrary, for the right position (B), $\varepsilon_{(110)}$ and $\varepsilon_{(131)/(041)}$ along the longitudinal direction increased and then showed constant values, whereas $\varepsilon_{(110)}$ and $\varepsilon_{(131/041)}$ along the transverse direction increased

and then decreased with increasing film strain. At the bottom position (C), an opposite trend to the right position was observed, but it appears to be consistent from the viewpoint of the circumference direction. In other words, $\varepsilon_{(110)}$ and $\varepsilon_{(131/041)}$ along the circumference direction for both positions (B) and (C) increased and showed constant values, whereas $\varepsilon_{(110)}$ and $\varepsilon_{(131/041)}$ along the radial direction

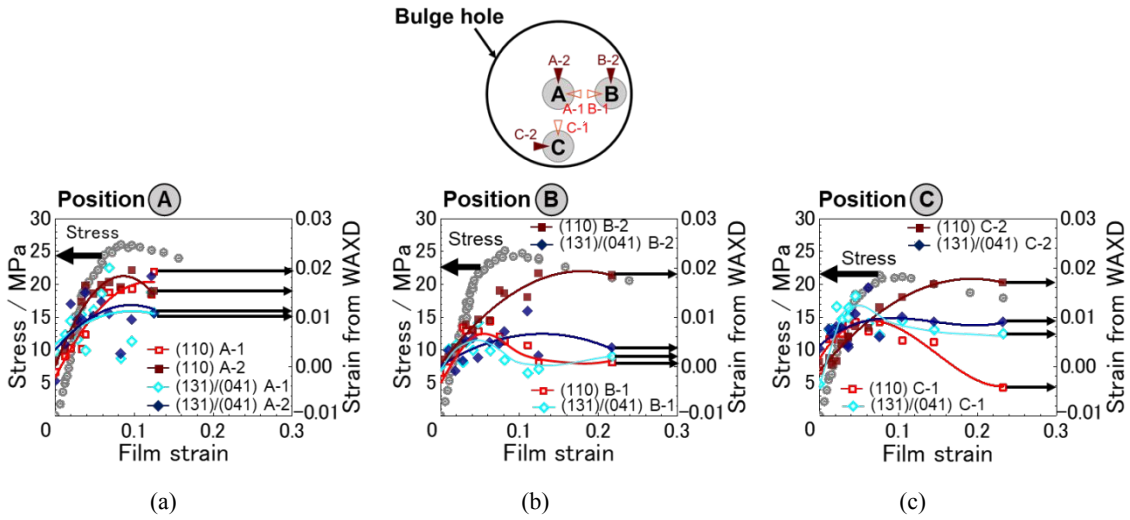

Figure 3. Relationship between film strain and strain obtained by WAXD profiles along transverse and longitudinal directions at three positions in the bulge hole. (a) center, (b) right, and (c) bottom.

increased and then decreased. These results imply that the stress direction is not considerably anisotropic in the initial film strain region below the yield point and obviously change to the circumference direction for positions (A), (B), and (C). Consequently, $\varepsilon_{(110)}$ and $\varepsilon_{(131/041)}$ along the transverse and longitudinal directions exhibited opposite trends in the high-strain region. This result corresponds well with the results obtained for poly (methyl methacrylate) films. [33]

Above yield point

Polarized high-speed camera observations were performed to clarify the macroscopic deformation behavior of the entire *it* PP film, as shown in Figure 1. Homogeneous colors were observed for both the retardation and direction of short-axis of the refractive index ellipsoid below a strain of 0.1, indicating that the *it* PP film was homogeneously deformed below the yield point ($\varepsilon <$ 0.06). An anisotropic craze began to form at approximately $\varepsilon = 0.12$. The number of crazes increased with the film strain, and the direction distribution of the long axis of the structure appeared to be isotropic. These formations appear to cancel the anisotropic stress that originates in the entire film. Figure 4 shows the polarized optical microscopic images of the *it* PP films after bulge testing. The images were recorded using POM with a 530 nm sensitive tint plate. Figure 4 (b) corresponds to a 90 ° rotation of the image shown in Figure 4 (a). The craze exhibited red and blue colors depending on the direction of its long axis. The color changes to blue and red correspond to $n_a > n_b$ and $n_b > n_a$, respectively. When the sample was rotated 90 °, the colors interchanged. Thus, it seems reasonable that the craze-like morphology possesses strong anisotropy because of the molecular orientation of the *it* PP chains. Considering the larger refractive index of *it* PP[34] in the molecular chain direction compared to that in the perpendicular direction, it is likely that the microfibrils are oriented perpendicular to the long axis of the craze-like morphology. Furthermore, the crashed region of the craze exhibits a purple color in Figure 4 and a blue color at a strain of 0.36 in Figure 1, corresponding to no retardation. This indicates that the orientation of the polymer chains disappeared

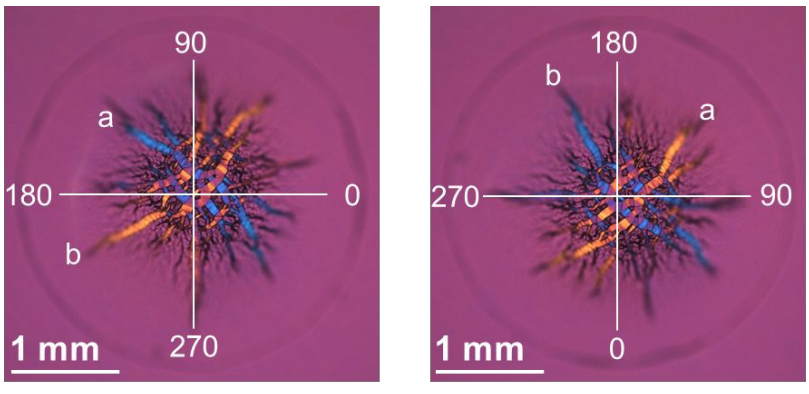

(a) (b)

Figure 4. Polarized optical microscopic image of the *it* PP films after bulge testing, obtained with a sensitive 530 nm tint plate. (a) 0 and (b) 90 degrees.

in the film plane via merging.

To clarify the molecular aggregation structure of the crazes, SAXS/WAXD measurements were performed on the *it* PP films after applying bulge deformation. Figure 5 shows the SAXS and WAXD patterns corresponding to the regions outside and inside the craze above the yield point. An obvious streak was observed at the craze in the SAXS pattern along with the direction of the long axis. This streak was not detected outside of the craze-like morphology. To understand the spatial distribution of crazes, ultra-small-angle X-ray scattering (USAXS) measurements were performed at 11 × 11 points. Figure S4 shows the USAXS patterns of the *it* PP films after bulge testing. The streaks were oriented radially from the center, supporting the discussion above. This indicates that microfibrils with sizes of 100 nm ~ 1 μm exist in the craze. In addition, an obvious Debye ring, which can be assigned to the (110) plane in the α phase of the *it* PP film, was observed, as shown in Figure 5 (d). This Debye ring disappeared at the craze, as shown in Figure 5 (e). This implies that the crystallites that formed in the entire *it* PP film changed to a different phase. Broad spots can be seen depending on the position of the craze. These broad spots correspond to the smectic phase[35-37] which consists of a pseudo-hexagonal lattice of *it* PP chains in the 3_1 helix conformation packed in

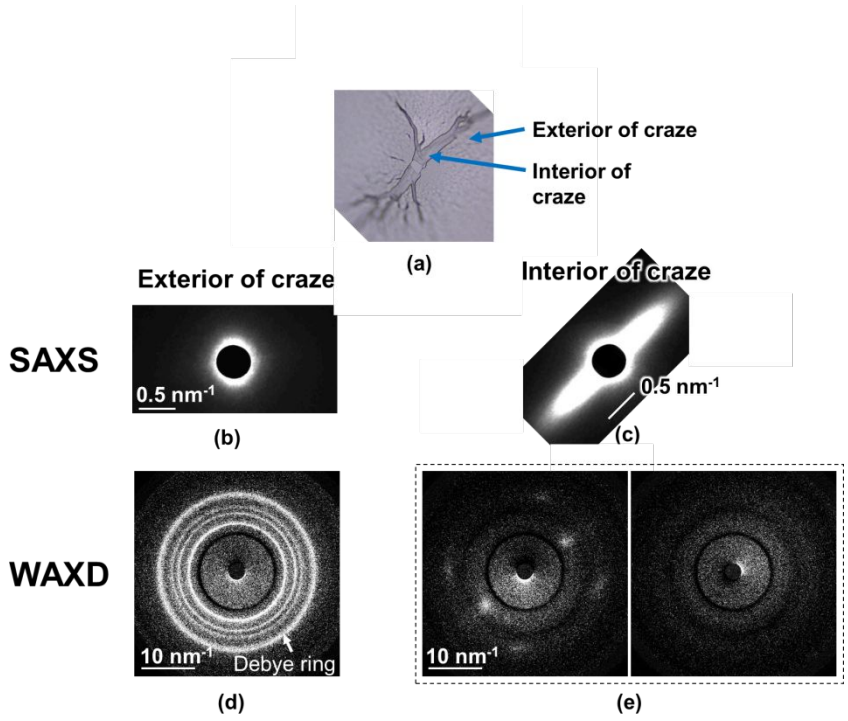

Figure 5. (a) Photograph of a craze; small-angle X-ray scattering (SAXS) patterns of (b) exterior and (c) interior of the craze; wide-angle X-ray diffraction (WAXD) patterns of the (d) exterior and (e) interior of the craze above the yield point.

the hexagonal lattice. Thus, it seems reasonable to conclude that *it* PP chains in the craze are in the smectic and amorphous phases.

Figure 6 shows high-speed-camera side-view images of the *it* PP films slightly before rupture under bulge deformation. The strain is ca. 0.36. In the side view, the shape is not an arc but is pointed, clearly indicating that plastic deformation has occurred. This corresponds well to the change in a side view shown in Figure S2. The curved line observed after rupture (right image) also implies that plastic deformation occurred. Moreover, the time required to form the rupture hole is around a single micro-second. A crack with a length of ca. 0.2 mm was observed after 2.4 μs (first red arrow). Thus, the crack growth rate of the *it* PP film can be roughly estimated ~80 m/s. The sound velocity, *v,* of *it* PP is approximately 1500 m/s. It is well-known that the crack growth rate, *a*, has the following relation with sound velocity: $a = 0.38\ v$,[38] and *a* is calculated as 580 m/s. Therefore, the crack growth rate obtained in the present bulge tests with high-speed-camera observations is reasonable because of a less decade difference. Since the specimen size for the bulge deformation test is small, it is easy to obtain the fracture behavior of the entire film. This is one of the most important features of the bulge test.

Figure 7 shows a schematic illustration of the change in the crystal lattice (left side) and macroscopic structure (right side) of the *it* PP films during bulge deformation. At the edge of the hole, as the film strain increased, the crystal lattice expanded isotropically below the yield point ($\sigma < \sigma_Y$). Then, the lattice strain along the circumferential and radial directions became larger and smaller above the yield point ($\sigma > \sigma_Y$). On the other hand, at the center of the hole, the crystal expanded isotropically below and above the yield point, indicating that a multiaxial stress occurred.

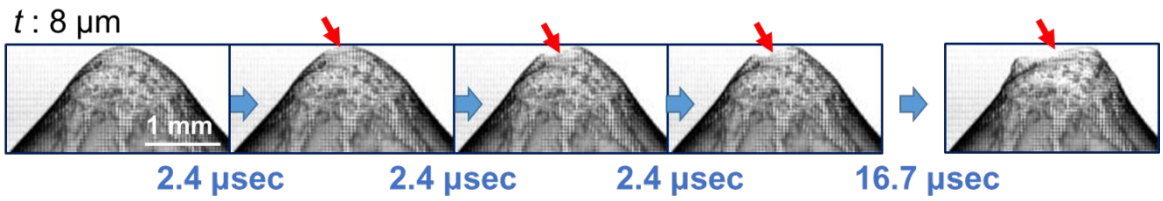

Figure 6. High-speed camera side-view images of *it* PP films during bulge deformation right before rupture.

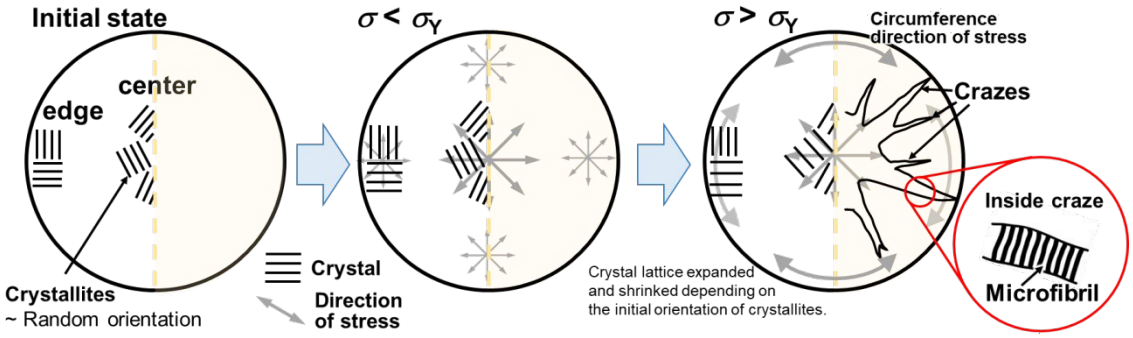

Figure 7. Schematic illustration of change in the crystal lattice, left side, and macroscopic structure change, right side of *it* PP films during bulge deformation.

Furthermore, randomly oriented crazes started to form above the yield point. Microfibrils in the crazes were packed in the smectic phase and oriented perpendicular to the long axis of the crazes.

Conclusions

A combination of the bulge deformation test and in situ molecular aggregation structure analyses was applied to crystalline *it* PP films. Below the yield point, isotropic expansion of the crystallites occurred at the center and edge of the hole. Above the yield point, the stress around the center of the film remained multiaxial, and uniaxial stress occurred along the circumferential direction. Macroscopically, crazes started to form in random directions. Owing to the high flexibility of the molecular chains of *it* PP and its string-shaped structure, biaxial and/or multiaxial stress fields spread by changing the anisotropic local uniaxial stress with the formation of anisotropic crazes. Inside the craze structure, *it* PP chains were in the smectic phase, forming 3_1 helical structures and microfibrils.

Acknowledgement

This work was supported by the Impulsing Paradigm Change through Disruptive Technology (ImPACT) Program, Japan Science and Technology Agency, PRESTO, Grant Number JPMJPR2194, JSPS KAKENHI Grant Number 21H02003. Synchrotron radiation X-ray scattering measurements were performed at BL05XU, BL40XU, and BL20XU in the SPring-8 facility with the approval of the Japan Synchrotron Radiation Research Institute (JASRI; Proposal No. 2016A1414, 2016B1436, 2015B1459, 2018B1035, 2019A1015, 2019B1011, 2021A1452). We gratefully

acknowledge Dr. Taiki Hoshino, Dr. So Fujinami, Dr. Tomotaka Nakatani, Mr. Kohki Aoyama, and Dr. Akihisa Takeuchi for their assistance with the WAXD measurements.

Uncategorized References

1. N. Pasquini, *Polypropylene Handbook second edition*, Carl Hanser Verlag GmbH & Co, 2005.
2. T. Kawai, S. Soeno, S.-i. Kuroda, S. Koido, T. Nemoto and M. Tamada, *Polymer*, 2019, **178**, 12123.
3. D. Lyu, Y. Lu, G. Thompson, F. Caton-Rose, Y. Lai, P. Coates and Y. Men, *Industrial & Engineering Chemistry Research*, 2021, **60**, 5151-5160.
4. Y. Lu, G. Thompson, D. Lyu, P. Caton-Rose, P. Coates and Y. Men, *Soft Matter*, 2018, **14**, 4432-4444.
5. B. Chang, K. Schneider, F. Xiang, R. Vogel, S. Roth and G. Heinrich, *Macromolecules*, 2018, **51**, 6276-6290.
6. X. Yang, T. Liao and Y. Men, *Polymer*, 2021, **219**, 123567.
7. X. Liu, L. Zou, B. Chang, H. Shi, Q. Yang, K. Cheng, T. Li, K. Schneider, G. Heinrich, C. Liu and C. Shen, *Polym. Test.*, 2021, **104**, 107404.
8. S. Nishitsuji, Y. Watanabe, T. Takebe, N. Fujii, M. Okano and M. Takenaka, *Polym. J.*, 2020, **52**, 279-287.
9. S. Nozaki, S. Masuda, C. H. Cheng, C. Nagano, K. Yokomachi, K. Kamitani, K. Aoyama, H. Masunaga, K. Kojio and A. Takahara, *ACS Macro Lett.*, 2019, **8**, 218-222.
10. T. Kida, Y. Hiejima and K. H. Nitta, *Express Polymer Letters*, 2016, **10**, 701-709.
11. Y. Nozue, Y. Shinohara, Y. Ogawa, T. Sakurai, H. Hori, T. Kasahara, N. Yamaguchi, N. Yagi and Y. Amemiya, *Macromolecules*, 2007, **40**, 2036-2045.
12. Y. Lin, W. Chen, L. Meng, D. Wang and L. Li, *Soft Matter*, 2020, **16**, 3599-3612.
13. K. Egoshi, T. Kanai and K. Tamura, *AIP Conf. Proc.*, 2017, **2055**, 060005.
14. C. H. Cheng, S. Masuda, S. Nozaki, C. Nagano, T. Hirai, K. Kojio and A. Takahara, *Macromolecules*, 2020, **53**, 4541-4551.
15. N. Dechnarong, K. Kamitani, C.-H. Cheng, S. Masuda, S. Nozaki, C. Nagano, Y. Amamoto, K. Kojio and A. Takahara, *Macromolecules*, 2020, **53**, 8901-8909.
16. N. Dechnarong, K. Kamitani, C.-H. Cheng, S. Masuda, S. Nozaki, C. Nagano, A. Fujimoto, A. Hamada, Y. Amamoto, K. Kojio and A. Takahara, *Polym. J.*, 2021, **53**, 703-712.
17. C. Nie, F. Peng, T. Xu, Y. Ding, J. Sheng, W. Chen and L. Li, *Macromolecules*, 2021, **54**, 9794-9803.
18. H. Tokumoto, H. Zhou, A. Takebe, K. Kamitani, K. Kojio, A. Takahara, K. Bhattacharya and K. Urayama, *Science Advances*, 2021, **7**.
19. K. Urayama, *Polym. Int.*, 2017, **66**, 195-206.
20. T. Kimura and K. Urayama, *ACS Macro Lett.*, 2019, **9**, 1-6.
21. T. Seto, T. Hara and K. Tanaka, *Jpn. J. Appl. Phys.*, 1968, **7**, 31-42.
22. M. K. Small, B. J. Daniels, B. M. Clemens and W. D. Nix, *J. Mater. Res.*, 1994, **9**, 25-30.
23. M. Trejo, V. Romero, E. Hamm and E. Cerda, *Soft Matter*, 2022, **18**, 762-767.

24. F. Su, W. Zhou, X. Li, Y. Ji, K. Cui, Z. Qi and L. Li, *Macromolecules*, 2014, **47**, 4408-4416.
25. C. Jiang, W. Y. Lio and V. V. Tsukruk, *Phys. Rev. Lett.*, 2005, **95**, 115503.
26. P. A. O'Connell and G. B. McKenna, *Science*, 2005, **307**, 1760-1763.
27. R. Vendamme, S. Y. Onoue, A. Nakao and T. Kunitake, *Nat. Mater.*, 2006, **5**, 494-501.
28. E. Ten, D. F. Bahr, B. Li, L. Jiang and M. P. Wolcott, *Ind. Eng. Chem. Res.*, 2012, **51**, 2941-2951.
29. H. Schlicke, E. W. Leib, A. Petrov, J. H. Schroder and T. Vossmeyer, *J. Phys. Chem. C*, 2014, **118**, 4386-4395.
30. H. Watanabe, A. Fujimoto, J. Nishida, T. Ohishi and A. Takahara, *Langmuir*, 2016, **32**, 4619-4623.
31. D. D. Kulkarni, I. Choi, S. S. Singamaneni and V. V. Tsukruk, *ACS Nano*, 2010, **4**, 4667-4676.
32. K. Kojio, C. Nagano, A. Fujimoto, S. Nozaki, K. Yokomachi, K. Kamitani, H. Watanabe and A. Takahara, *Soft Matter*, 2018, **14**, 1659-1664.
33. K. Kojio, A. Fujimoto, T. Kajiwara, C. Nagano, S. Masuda, C.-H. Cheng, S. Nozaki, K. Kamitani, H. Watanabe and A. Takahara, *Polymer*, 2019, **179**, 121632.
34. S. S. Hardaker, S. Moghazy, C. Y. Cha and R. J. Samuels, *J. Polym. Sci., Part B: Polym. Phys.*, 1993, **31**, 1951-1963.
35. G. Natta, *Die Makromolekulare Chemie*, 1960, **35**, 94-131.
36. S. Minami, Y. Tanoue and M. Takayanagi, *Kogyo Kagaku Zasshi*, 1965, **68**, 830.
37. T. Konishi, K. Nishida and T. Kanaya, *Macromolecules*, 2006, **39**, 8035-8040.
38. J. J. Gilman, *J. Appl. Phys.*, 1956, **27**, 1262-1269.